Available online at www.sciencedirect.com

SciVerse ScienceDirect

Ceramics International 39 (2013) 5909–5917

CERAMICS INTERNATIONAL

www.elsevier.com/locate/ceramint

Microwave combustion synthesis, structural, optical and magnetic properties of $Zn_{1-x}Sr_xFe_2O_4$ nanoparticles

A. Manikandan[a], J. Judith Vijaya[a,*], L. John Kennedy[b], M. Bououdina[c,d]

[a]*Catalysis and Nanomaterials Research Laboratory, Department of Chemistry, Loyola College, Chennai 600034, India*
[b]*Materials Division, School of Advanced Sciences, Vellore Institute of Technology University, Chennai Campus, Chennai 600127, India*
[c]*Department of Physics, College of Science, University of Bahrain, PO Box 32038, Kingdom of Bahrain*
[d]*Nanotechnology Centre, University of Bahrain, PO Box 32038, Kingdom of Bahrain*

Received 12 September 2012; received in revised form 4 January 2013; accepted 5 January 2013
Available online 23 January 2013

Abstract

Pure and strontium doped zinc ferrite ($Zn_{1-x}Sr_xFe_2O_4$) nanoparticles were prepared by the microwave combustion method using urea as the fuel. Rietveld refinements of X-ray diffraction pattern confirm the formation of single cubic spinel phase with an average crystallite size in the range of 25–42 nm. The broad visible emission band is observed in the entire photoluminescence spectrum. The estimated band gap energy is found to decrease with increasing Sr content, i.e. 2.1–1.72 eV. Magnetic measurements at room temperature revealed that at lower Sr concentration ($x \leq 0.2$), the system shows a superparamagnetic behavior, whereas at higher Sr concentration ($x \geq 0.2$), it becomes ferromagnetic. The relatively high saturation magnetization of the as-prepared Sr-doped $ZnFe_2O_4$ nanoparticles suggest that this method is suitable for preparing high-quality nanocrystalline magnetic ferrites for practical applications. The mechanism for the formation of $ZnFe_2O_4$ by the microwave combustion method is also discussed in the present study. Microwave combustion produced sufficient energy for the formation of $ZnFe_2O_4$, because of its homogeneous distribution within the raw materials. This results in the formation of nanoparticles and early phase formation within few minutes of time.

Keywords: Zinc ferrites; Nanoparticles; Optical properties; C. Magnetic properties

1. Introduction

Spinel ferrite nanoparticles exhibit unique physical and magnetic properties, due to the quantum confinement when compared to bulk materials [1]. Ferrite nanoparticles become more important in biotechnology and biomedicine, as well as in technical areas like magnetic data storage over the past few years [2]. Spinel ferrites with a general formula AFe_2O_4 (A= divalent cation, Mn^{2+}, Fe^{2+}, Co^{2+}, Ni^{2+}, Zn^{2+}, etc.) have been investigated for their usual electrical and magnetic properties. For the normal spinel ferrites, all the divalent cations occupy the tetrahedral sites and the trivalent cations occupy the octahedral sites. The magnetic property of a spinel phase is very sensitive to the type of cations and their distribution in the interstitial sites (tetrahedral and octahedral) of the spinel lattice [3]. Zinc ferrite ($ZnFe_2O_4$) in bulk form shows a normal spinel structure with zinc ions located at tetrahedral sites and iron ions at octahedral sites [4,5]. It is a commercially important material and has been widely used in many areas, such as magnetic applications [6], gas sensors [7], catalysts [8], photo-catalysts [9] absorbent materials [10], information storage and electronic devices [11]. The electrical and magnetic properties of Zn ferrites are highly sensitive to the cations distribution, preparation conditions and substitution of different transition metals. Several methods have been used to prepare $ZnFe_2O_4$ nanostructures, including sol–gel [12], high-energy ball milling [6], hydro-thermal [8], co-precipitation [13], ferrocenyl precursor [14], ultrasonic cavitation [15] and thermal plasma [16] methods, etc. However, the above methods encounter some disadvantages such as, the requirement of

*Corresponding author. Tel.: +91 44 28178200; fax: +91 44 28175566.
E-mail addresses: jjvijayaloyola@yahoo.co.in, jjvijaya78@gmail.com (J. Judith Vijaya).

0272-8842/$ - see front matter © 2013 Elsevier Ltd and Techna Group S.r.l. All rights reserved.
http://dx.doi.org/10.1016/j.ceramint.2013.01.012

complicated equipment, higher processing temperature, high-energy consuming and also require rather long reaction time caused by the multiple steps to complete the crystallization of $ZnFe_2O_4$ nanostructures.

However, the microwave combustion method (MCM) has recently gained importance than the above said methods. In MCM approach, the microwaves interact with the reactants at the molecular level, which leads to a uniform heating. During the microwave combustion, the microwave energy is transferred and converted to heat because of the motion of the molecules. This results in the formation of $ZnFe_2O_4$ nanoparticles within few minutes of time and leads to a higher efficiency [17].

In this work, we have synthesized pure and Sr-doped $ZnFe_2O_4$ nanoparticles by the microwave combustion method. The structural phase of the prepared samples was characterized by X-ray diffraction (XRD) analysis. The particle size and morphologies were determined by high resolution scanning electron microscopy (HR-SEM) and the chemical composition was determined by the energy dispersive X-ray analysis (EDX). The magnetic behavior of the samples was studied by the vibrating sample magnetometer (VSM). The effect of doping Sr^{2+} ions concentration on various properties of zinc ferrite, like structural, morphological, optical and magnetic properties have been investigated.

2. Experimental

2.1. Materials and methods

All the chemicals used in this study were of analytical grade obtained from Merck, India and were used as received without further purification. Zinc nitrate ($Zn(NO_3)_2 \cdot 6H_2O$, 98%), ferric nitrate ($Fe(NO_3)_3 \cdot 9H_2O$, 98%) and strontium nitrate ($Sr(NO_3)_2$) were used as precursors and urea as a fuel for this reaction. The compositions were prepared with the addition of strontium of different molar ratios ($Zn_{1-x}Sr_xFe_2O_4$ with $x=0.0$, 0.1, 0.2, 0.3, 0.4 and 0.5) to $ZnFe_2O_4$. For the preparation of pure zinc ferrite using the microwave combustion technique, the precursor mixture in urea was placed into a domestic microwave oven and exposed to the microwave energy in a 2.45 GHz multimode cavity at 750 W for 10 min. After the completion of the reaction, the solid powder was obtained and then it was washed with ethanol and dried at 70 °C for 1 h. The obtained powders were labeled as ZnSF1, ZnSF2, ZnSF3, ZnSF4, ZnSF5 and ZnSF6.

The entire microwave combustion process produces zinc ferrite powders in a microwave-oven operated at a power of 750 W has produced a temperature ranging from 150 to 400 °C that would have resulted in the formation of $ZnFe_2O_4$ within 10 min [18]. The expected combustion reaction may be as follows:

$$2Zn(NO_3)_2 \cdot 6H_2O_{(S)} + 4Fe(NO_3)_3 \cdot 9H_2O_{(S)} + 4CO(NH_2)_{2(S)} + 2O_{2(g)} \rightarrow 2ZnFe_2O_{4(S)} + 56H_2O_{(g)}\uparrow + 4CO_{2(g)}\uparrow + 4N_{2(g)}\uparrow + 16NO_{2(g)}\uparrow$$

2.2. Characterizations

The structural characterization of pure and Sr-doped $ZnFe_2O_4$ nanoparticles were performed using a Rigaku Ultima X-ray diffractometer equipped with Cu-Kα radiation ($\lambda=1.5418$ Å). Structural refinements using the Rietveld method was carried out using PDXL program; both refined lattice parameters and crystallite size of the obtained ferrites were reported. Morphological studies and energy dispersive X-ray analysis of pure and Sr-doped $ZnFe_2O_4$ nanoparticles have been performed with a Jeol JSM6360 high resolution scanning electron microscope (HR-SEM). The diffuse reflectance UV–visible spectrum (DRS) was recorded using Cary100 UV–visible spectrophotometer to estimate their band gap energy. The photoluminescence (PL) properties were recorded using Varian Cary Eclipse Fluorescence Spectrophotometer. Magnetic measurements were carried out at room temperature using a PMC MicroMag 3900 model vibrating sample magnetometer (VSM) equipped with 1 T magnet.

3. Results and discussion

3.1. XRD analysis

The X-ray diffraction patterns of $Zn_{1-x}Sr_xFe_2O_4$ system ($x=0.0$, 0.1, 0.2, 0.3, 0.4 and 0.5) are shown in Fig. 1a–f.

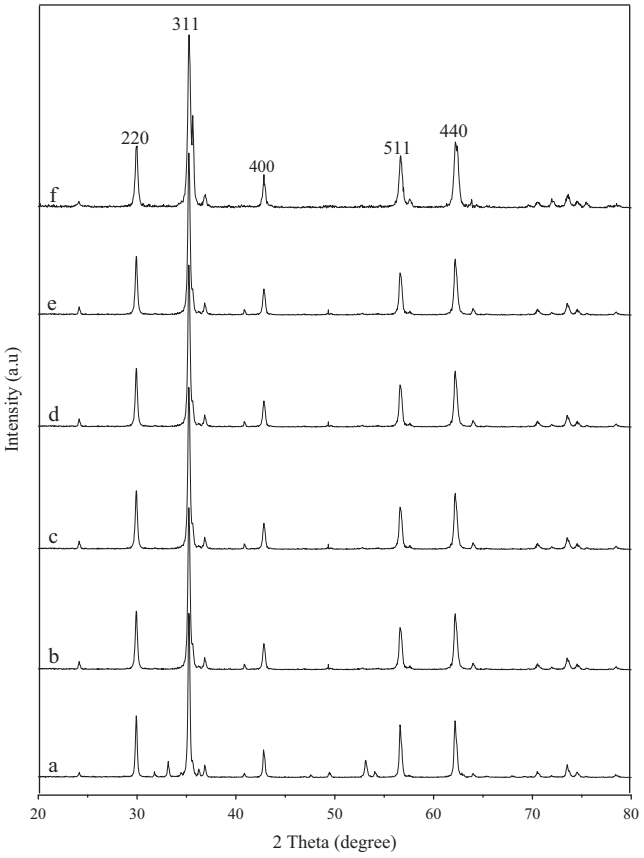

Fig. 1. XRD patterns of (a) ZnSF1, (b) ZnSF2, (c) ZnSF3, (d) ZnSF4, (e) ZnSF5 and (f) ZnSF6 systems.

It can be observed that all the peaks of pure as well as Sr-doped $ZnFe_2O_4$ powders can be easily indexed with cubic $ZnFe_2O_4$ spinel structure (JCPDS no. 22-1012). The diffraction peaks at 2θ values 29.99°, 35.24°, 42.83°, 56.65° and 62.19° can be ascribed to the reflections (220), (311), (400), (511) and (440) planes of the spinel crystal structure, respectively. There is no additional peak for all compositions, which indicates that all the samples crystallize in single-phase cubic structure with Fd3m space group [19]. In addition, the crystallite size is estimated from the most intense (311) reflection peak using the Debye Scherrer formula [20]. The crystallite size of ZnSF1, ZnSF2, ZnSF3, ZnSF4, ZnSF5 and ZnSF6 were found to be 42, 38, 31, 28, 27 and 25 nm respectively. It shows clearly that by increasing the amount of Sr^{2+} ions, the crystallite size decreases. The reduction of crystallite size with increasing Sr content may be due to the requirement of high energy for Sr^{2+} ions to enter into the $ZnFe_2O_4$ lattice [21].

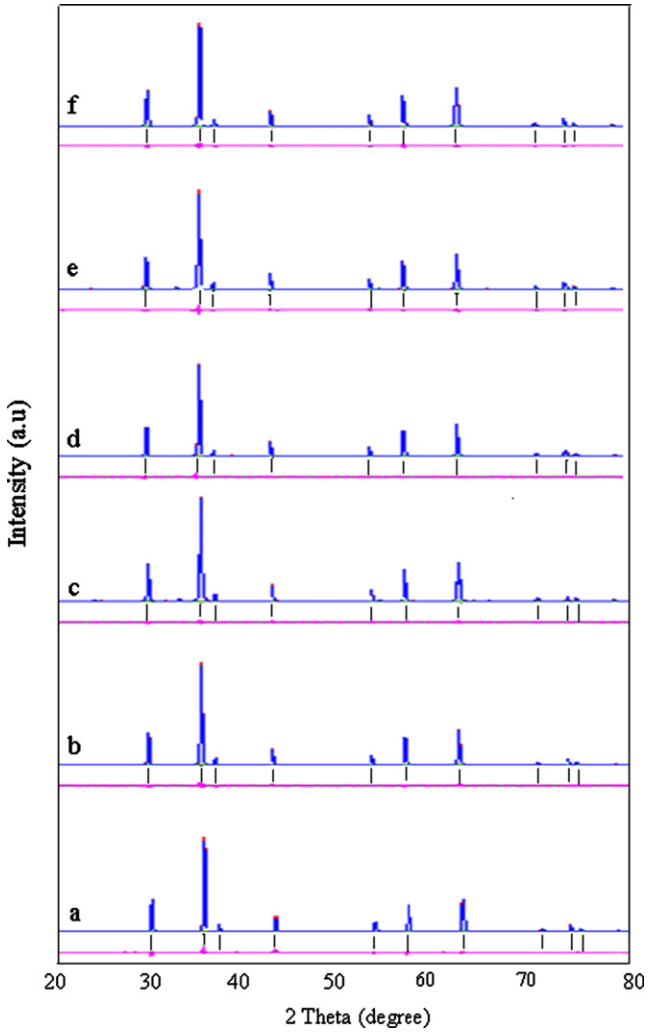

Fig. 2. XRD pattern refinements using the Rietveld method of (a) ZnSF1, (b) ZnSF2, (c) ZnSF3, (d) ZnSF4, (e) ZnSF5 and (f) ZnSF6 systems. (Experimental data, upper solid line: calculated pattern, lower solid line: intensity difference: Bragg reflection positions).

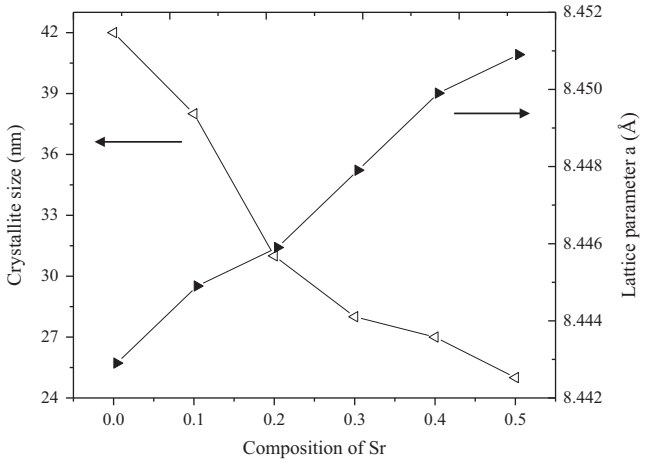

Fig. 3. Evolution of the lattice constant and crystallite size of $Zn_{1-x}Sr_xFe_2O_4$ (x=0.0, 0.1, 0.2, 0.3, 0.4 and 0.5) system.

Several techniques have been used to characterize the cubic spinel ferrites in order to understand their intrinsic magnetic properties. Rietveld analysis is a powerful method to determine both structural and microstructural parameters including site occupancy. The profile of X-ray diffraction data is fitted using the Rietveld analysis and the corresponding spectra are given in Fig. 2. It was designed to refine simultaneously, the lattice cell constant, atomic position, occupancy, crystallite size and lattice strain. In Fig. 2, the calculated patterns are shown in the same field as a solid line curve. The difference observed minus calculated is shown in the lower field. The short vertical bars in the middle field indicate the positions of possible Bragg reflections. The lattice parameter of pure $ZnFe_2O_4$ is found to be equal to 8.443 Å, which is in good accordance with the standard JCPDS value of 8.441 Å (JCPDS no. 22-1012) and comparable to the reported values in literature, a=8.445 Å [22] and a=8.449 Å [23]. Moreover, the condition was imposed that the quantity of Fe^{3+} ions migrating from B-sites (octahedral) to A-sites (tetrahedral) is the same as the quantity of Zn^{2+} ions are migrating in reverse order. The lattice parameter is found to increase almost linearly with increasing Sr content. The values of the crystallite size and the lattice parameter for pure and Sr doped $ZnFe_2O_4$ samples are reported in Fig. 3 and Table 1. During the refinements, the goodness of fit is defined by the reliability factor $S=R_{wp}/R_e$, where R_{wp} and R_e, are, respectively, the R-weighted and the R-expected patterns. The difference in the values of the lattice parameter and crystallite size may be affected by several factors including the preparation method, molar ratio of the starting precursors and the nature of precursors, etc. The values of the crystallite size obtained by both Rietveld and Scherrer methods are shown in Table 1.

However, in the present study, the value of the lattice parameter is increased from 8.443 Å to 8.451 Å with increasing the Sr^{2+} content. It is because of the fact that Sr^{2+} (1.44 Å) ion has larger ionic radius than Zn^{2+}

Table 1
Lattice parameter, crystallite size (Scherrer formula, Rietveld analysis) and band gap values of $Zn_{1-x}Sr_xFe_2O_4$ (x=0.0, 0.1, 0.2, 0.3, 0.4 and 0.5) system.

Samples	Lattice parameters (Å) Rietveld analysis	Crystallite size D (nm)		Band gap (eV)	Strain (%)	S (Goodness of fit)
		Scherrer formula	Rietveld analysis			
ZnSF1	8.443	42	43	2.1	0.067	1.18
ZnSF2	8.445	38	35	1.95	0.069	1.13
ZnSF3	8.446	31	32	1.92	0.070	1.11
ZnSF4	8.448	28	29	1.84	0.072	1.09
ZnSF5	8.450	27	25	1.76	0.075	1.10
ZnSF6	8.451	25	23	1.72	0.077	1.14

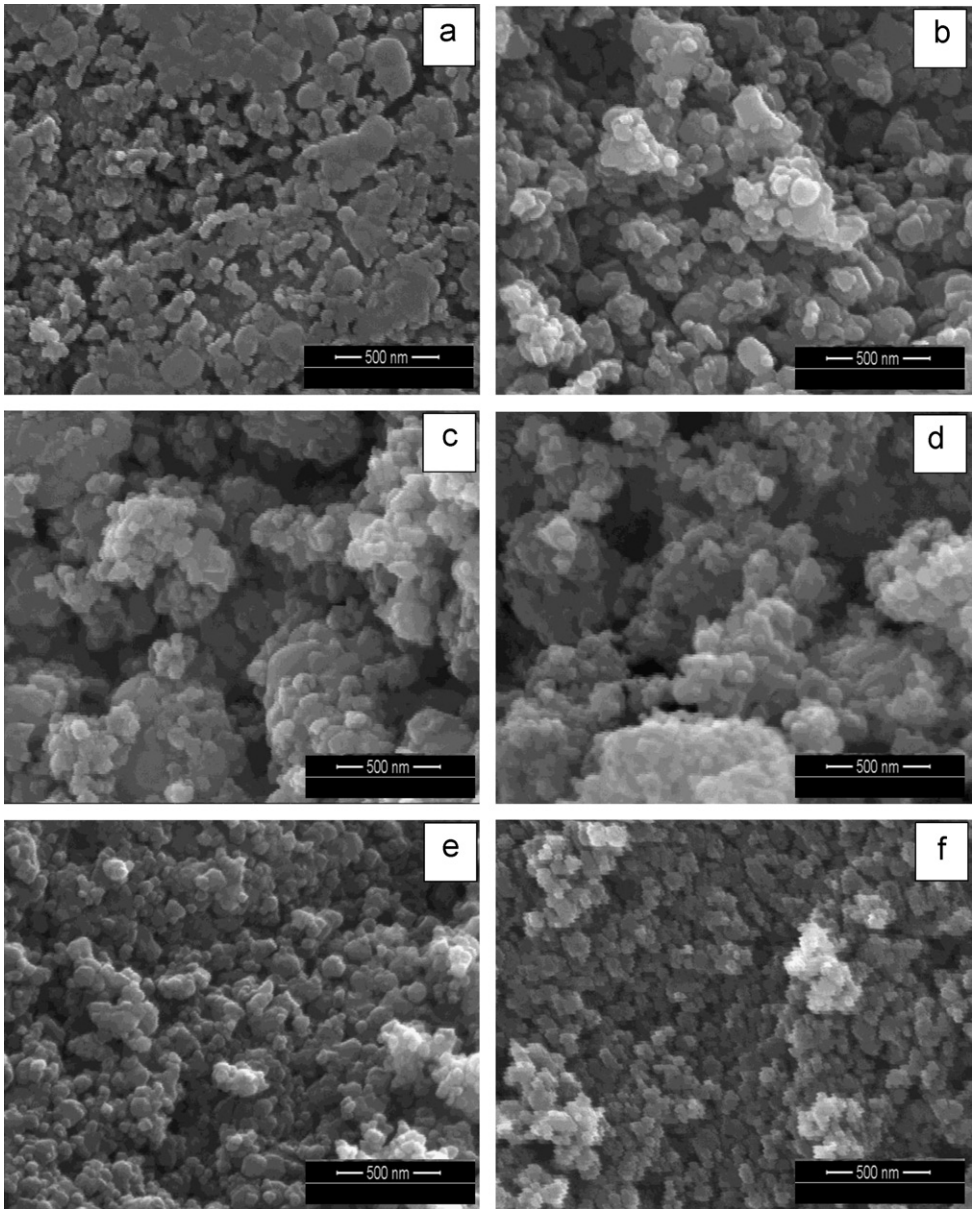

Fig. 4. HR-SEM images of (a) ZnSF1, (b) ZnSF2, (c) ZnSF3, (d) ZnSF4, (e) ZnSF5 and (f) ZnSF6 systems.

(0.83 Å) ion; the increase in Sr substitution content consequently results in lattice expansion [24]. It is to be noted that as the Sr content increases, strain induced inside the sample also increases, thus obeying Vegard's law [25–27]. The values of strain are listed in Table 1. It is found that the strain is lower for pure zinc ferrite and increases with increase in Sr^{2+} content. A linear increase of the lattice spacing thus indicates that Sr^{2+} ions with higher ionic

radius are replacing Zn^{2+} ions with smaller ionic radius in Zn ferrite crystal lattice. Tangcharoen et al. [28] also reported that the lattice parameter increases with increase in doping concentrations, and is in good agreement with the results obtained in this study.

3.2. Scanning electron microscopy studies

Fig. 4(a–f) shows the high resolution scanning electron microscopy (HR-SEM) images of pure and Sr-doped $ZnFe_2O_4$ nanoparticles. From the images, one can notice the formation of spherical and uniform particles. The average particle size of the ferrite nanoparticles prepared via this route is found to be in the range of 43–22 nm. With increase in Sr doping, the spacing between the particles are expected to become narrower and also there is a decrease in particle size, which confirms that the presence of Sr^{2+} obstructs the crystal growth [29]. The formation of Sr-doped zinc ferrite is more exothermic when compared to the formation of pure zinc ferrite. Thus, it is expected that when Sr^{2+} is introduced in the system, more heat will be liberated with direct crystallization, and hence obstructing the grain growth [30,31]. Similar results were reported in literature [32]. These values are in good agreement with Rietveld analysis results. The observed slight difference in particle size values as estimated from the two different techniques (XRD and HR-SEM) may be due to some structural disorder and strain in the lattice resulted from different ionic radii and/or clustering of the nanoparticles.

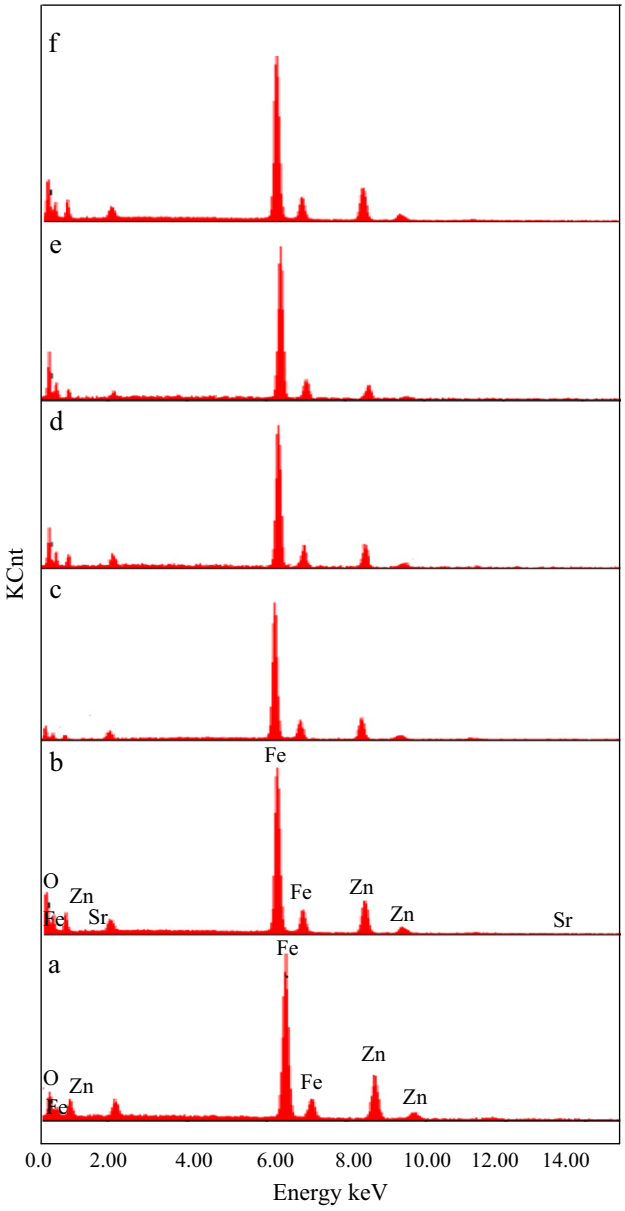

Fig. 5. EDX spectra of (a) ZnSF1, (b) ZnSF2, (c) ZnSF3, (d) ZnSF4, (e) ZnSF5 and (f) ZnSF6 systems.

3.3. Energy dispersive X-ray analysis (EDX)

EDX spectra of the respective samples are shown in Fig. 5(a–f). The peaks corresponding to the elements Fe, Zn and O were observed in pure $ZnFe_2O_4$ (Fig. 5a) and the peaks of the elements Fe, Zn, Sr and O were observed in Sr-doped $ZnFe_2O_4$ system (Fig. 5(b–f)). The observed percentage of Sr and Zn values matches well with the amounts of Sr and Zn used in the respective precursors (Table 2). The signal of Cu originates from the copper grid. Moreover, the microwave combustion method is very effective, because no loss of elements occurred during the synthesis.

3.4. Optical properties by diffuse reflectance spectroscopy (DRS)

The optical properties of pure and Sr-doped $ZnFe_2O_4$ nanoparticles were investigated at room temperature by using UV–visible diffuse reflectance spectroscopy (DRS). Fig. 6 shows the Kubelka-Munk reflectance spectra of pure and Sr-doped $ZnFe_2O_4$. In order to assign the band gap with certainty, the diffuse reflectance (R) of the samples were transformed using Kubelka-Munk function F(R). The definition of Kubelka-Munk function [33,34] is

Table 2
Energy dispersive X-ray analysis (EDX) results of $Zn_{1-x}Sr_xFe_2O_4$ (x=0.0, 0.1, 0.2, 0.3, 0.4 and 0.5) system.

Samples	Elements	Zn	Sr	Fe	O	Total%
ZnSF1	Wt%	32.95	–	57.41	09.64	100
	At%	23.61	–	48.16	28.23	
ZnSF2	Wt%	30.22	03.22	57.24	09.32	100
	At%	21.77	02.57	48.25	27.42	
ZnSF3	Wt%	26.64	06.56	57.05	09.75	100
	At%	18.96	05.17	47.51	28.36	
ZnSF4	Wt%	22.77	09.10	54.79	13.33	100
	At%	15.03	06.67	42.34	35.96	
ZnSF5	Wt%	18.89	11.98	53.87	15.26	100
	At%	11.98	08.43	40.01	39.58	
ZnSF6	Wt%	15.86	15.00	56.78	12.36	100
	At%	10.61	11.14	44.47	33.78	

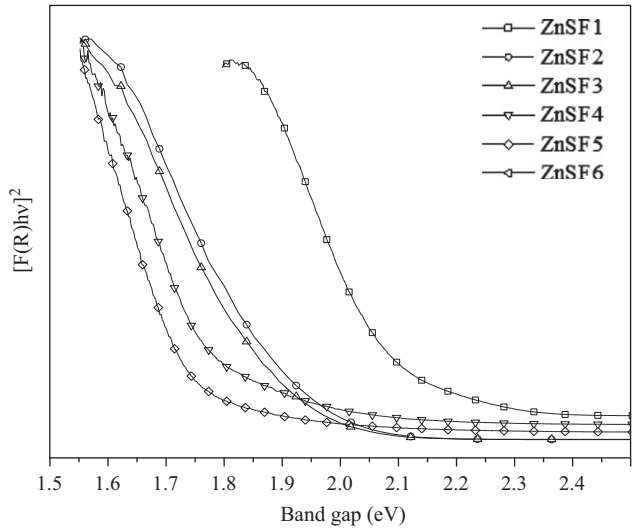

Fig. 6. UV–visible reflectance spectra of $Zn_{1-x}Sr_xFe_2O_4$ (x=0.0, 0.1, 0.2, 0.3, 0.4 and 0.5) system.

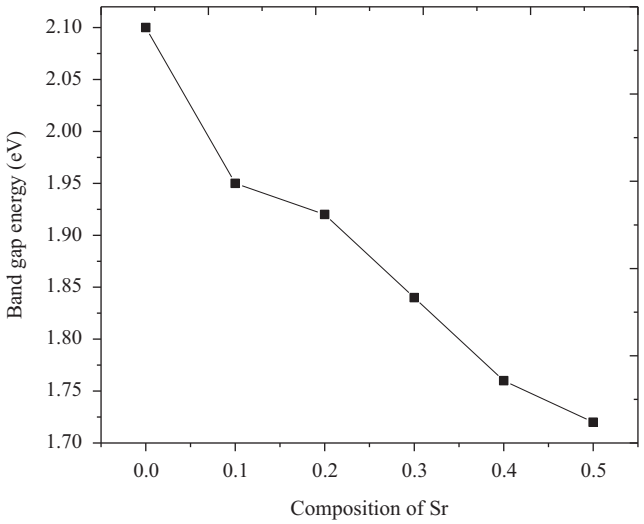

Fig. 7. Variation of the band gap energy of $Zn_{1-x}Sr_xFe_2O_4$ (x=0.0, 0.1, 0.2, 0.3, 0.4 and 0.5) system.

enumerated as follows:

$$F(R) = (1-R)^2/2R \quad (1)$$

Fig. 7 shows the variation of band gaps of the samples ZnSF1 (2.1 eV), ZnSF2 (1.95 eV), ZnSF3 (1.92 eV), ZnSF4 (1.84 eV), ZnSF5 (1.76 eV) and ZnSF6 (1.72 eV). Fig. 7 shows that there is a decrease in the band gap of the Sr-doped $ZnFe_2O_4$ samples, when compared to the pure $ZnFe_2O_4$. The E_g value of typical $ZnFe_2O_4$ is 1.9 eV, and hence there is a blue shift for ZnSF1, ZnSF2, ZnSF3 and red shift for ZnSF4, ZnSF5, ZnSF6 samples. This may be due to the additional sub-band-gap energy levels that are induced by the abundant surface and interface defects in the agglomerated nanoparticles [35,36]. However, the band

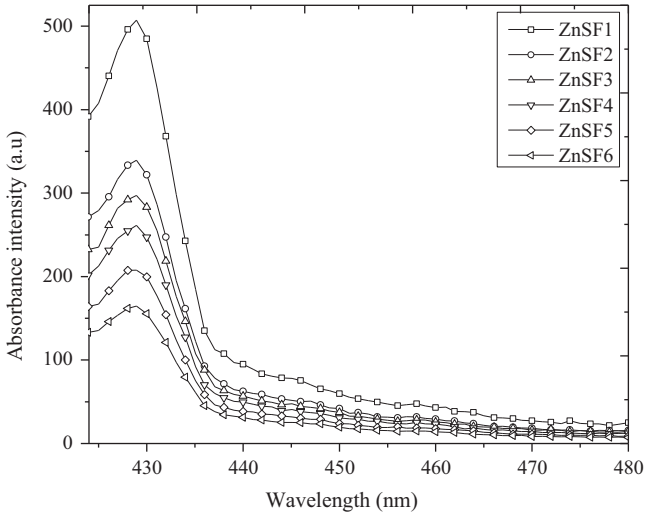

Fig. 8. PL spectra of $Zn_{1-x}Sr_xFe_2O_4$ (x=0.0, 0.1, 0.2, 0.3, 0.4 and 0.5) system.

gap value decreases with increasing Sr content, and is due to the difference in the electronic structure of the dopant.

3.5. Photoluminescence (PL) studies

Fig. 8 shows the room temperature photoluminescence (PL) spectra of pure and Sr-doped $ZnFe_2O_4$ samples. The samples were excited using the excitation wavelength of 414 nm. All the samples show the characteristic near-band-edge (NBE) emission of pure and Sr-doped $ZnFe_2O_4$ at around 428 nm. A broader visible emission band was obtained for all the samples centered at 428 nm, and is attributed to the recombination of electrons deeply trapped in oxygen vacancies with photogenerated holes [37]. This band may also be due to the charge transfer between Fe^{3+} ions at octahedral sites and Zn^{2+} ions at tetrahedral sites, which are surrounded by O^{2-} ions [38,39]. The PL emission of zinc ferrite samples is attributed to the presence of more structural defects on the crystal lattice, the appearance of new electronic levels between the conduction and the valence bands and it might be due to the increase in the interstitial defects [40–42]. The intensity of the emission bands decreased toward lower energies as the particle size was decreased, which might be related to the quantum confinement effect [43].

3.6. VSM measurements

Fig. 9 shows the VSM measurements of $Zn_{1-x}Sr_xFe_2O_4$ samples carried out at room temperature with applied field ranging from −10 to +10 kOe. $ZnFe_2O_4$ is a soft magnetic material. When Zn^{2+} in $ZnFe_2O_4$ is substituted by Sr^{2+} ions, there is drastic change in magnetic properties like saturation magnetization (M_s), remanent magnetization (M_r) and coercivity (H_c). The variation in magnetic property of the samples is shown in Fig. 10(a–c) and the

values are reported in Table 3. The ZnSF1, ZnSF2 and ZnSF3 samples with lesser Sr concentration ($x \leq 0.2$) show paramagnetic behavior. This indicates that Zn^{2+} ions occupying the tetrahedral sites and Fe^{3+} ions the octahedral sites, whereas the dopant Sr^{2+} ions occupy either octahedral or tetrahedral sites [44], thus showing a paramagnetic behavior. Similar results were reported in literature [45].

The M_s values of samples ZnSF4, ZnSF5 and ZnSF6 are 20.93, 38.75 and 59.58 emu/g, respectively. There is increase in the ferromagnetic behavior for ZnSF4, ZnSF5 and ZnSF6 samples with increase in Sr^{2+} concentration ($x \geq 0.2$). The change in the value of M_s is most probably due to the difference in the cation sharing at the tetrahedral and octahedral sites [46]. The ferromagnetic behavior is absent in ZnSF1, ZnSF2 and ZnSF3 samples, and this may be due to the non-equilibrium distribution of Fe^{3+} ions in tetrahedral and octahedral sites, which is in good agreement with some previous reports [44,47–49]. M_s

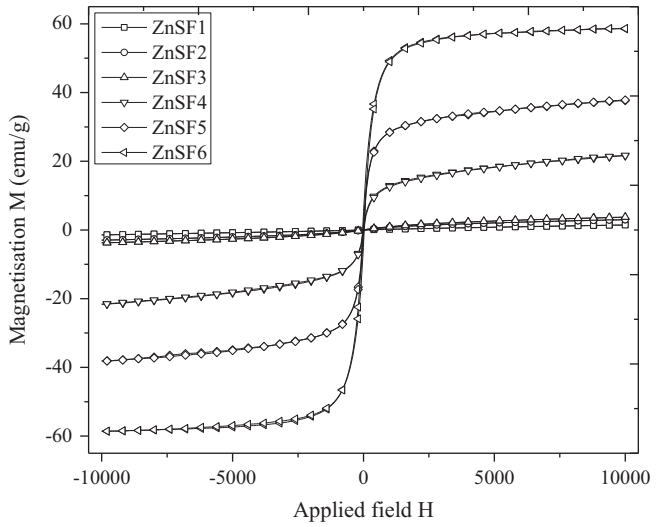

Fig. 9. Magnetic hysteresis loops of $Zn_{1-x}Sr_xFe_2O_4$ (x=0.0, 0.1, 0.2, 0.3, 0.4 and 0.5) system.

Table 3
Magnetic properties (magnetization, remanence and coercivity) of $Zn_{1-x}Sr_xFe_2O_4$ (x=0.0, 0.1, 0.2, 0.3, 0.4 and 0.5) system.

Samples	H_c (Oe)	M_r (emu/g)	M_s (emu/g)
ZnSF1	5.027	0.0016	1.638
ZnSF2	8.192	0.0145	2.979
ZnSF3	10.132	0.0936	3.749
ZnSF4	14.831	0.8852	20.932
ZnSF5	16.682	2.1672	38.751
ZnSF6	30.152	4.6562	59.581

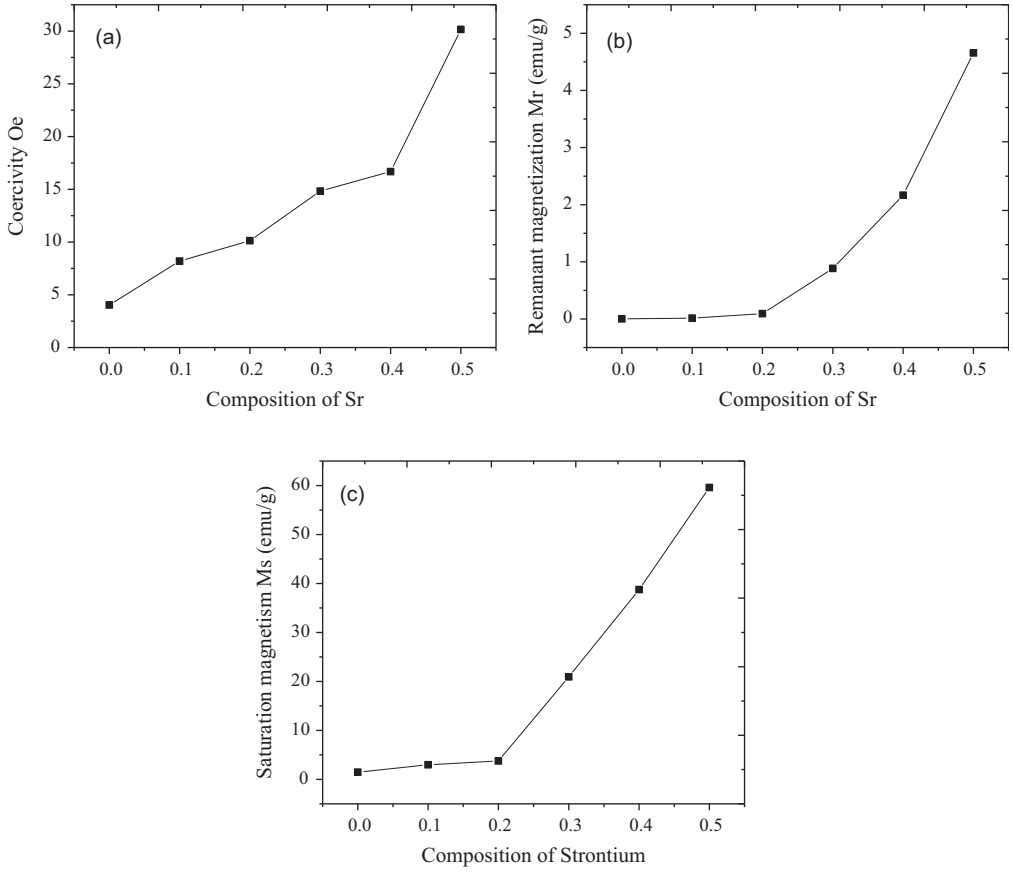

Fig. 10. Magnetic properties of $Zn_{1-x}Sr_xFe_2O_4$ (x=0.0, 0.1, 0.2, 0.3, 0.4 and 0.5) system: (a) Coercivity, (b) Remanant magnetization, (c) Saturation magnetization.

values strongly depend on various factors such as the synthesis route and its conditions, type of the precursors and subsequent treatments, etc.

The non-saturation observed in MH loop and the absence of the hysteresis, M_r and H_c indicate that ZnSF1, ZnSF2 and ZnSF3 samples have superparamagnetic behavior [20]. Moreover, the very low values of H_c and M_r, indicate that they are also soft magnets [50–52]. The lattice parameter of the samples ZnSF1, ZnSF2, ZnSF3, ZnSF4, ZnSF5 and ZnSF6 increased from 8.443 Å to 8.451 Å due to Sr-doping, leading to the expansion of the unit cell volume, which in turn increase the inter-atomic distance between the ions and affects the magnetic properties.

4. Conclusions

Nano-sized pure and Sr-doped zinc ferrites were successfully prepared by the microwave combustion method using urea as the fuel. This method allows synthesizing the spinel structure with good crystallinity and reproducibility. The crystallite size was found to vary within the range of 25–42 nm. The formation of pure spinel phase was confirmed by Rietveld analysis. The crystallite size decreases and the lattice parameter increases with increasing Sr content, which may be attributed to a possible redistribution of Zn^{2+} and Fe^{3+} ions within tetrahedral and octahedral sites. UV–visible absorption spectroscopy shows that the band gap energy of the pure $ZnFe_2O_4$ nanoparticle is 2.1 eV, which then decreases with increasing Sr-doping. Magnetic measurements of $Zn_{1-x}Sr_xFe_2O_4$ nanoparticles revealed that, at lower Sr concentration ($x \leq 0.2$), the system shows a superparamagnetic behavior, whereas at higher concentration ($x \geq 0.2$), it becomes ferromagnetic.

References

[1] M. Zheng, X.C. Wu, B.S. Zou, Y.J. Wang, Magnetic properties of nanosized $MnFe_2O_4$ particles, Journal of Magnetism and Magnetic Materials 183 (1998) 152–156.

[2] O.T.B. Ulrich, I.T. Michael, G. Kaul, M.S. Nikolic, B. Mollwitz, R.A. Sperling, R. Reimer, H. Hohenberg, W.J. Parak, S.F.G. Adam, H. Weller, N.C. Bigall, Size and surface effects on the MRI relaxivity of manganese ferrite nanoparticle contrast agents, Nano Letters 7 (2007) 2422–2427.

[3] B.D. Cullity, Introduction to Magnetic Materials, Addison-Wesley, New York, 1972.

[4] T. Sato, K. Haneda, M. Seki, T. Iijima, Morphology and magnetic properties of ultrafine $ZnFe_2O_4$ particles, Applied Physics A 50 (1990) 13–16.

[5] C.N. Chinnasamy, A. Narayanasamy, N. Ponpandian, K. Chattopadhyay, H. Guerault, J.M. Greneche, Magnetic properties of nanostructured ferrimagnetic zinc ferrite, Journal of Physics Condensed Matter 12 (2000) 7795–7805.

[6] H. Ehrhardt, S.J. Campbell, M. Hofmann, Magnetism of the nanostructured spinel zinc ferrite, Scripta Materialia 48 (2003) 1141–1146.

[7] N. Ikenaga, Y. Ohgaito, H. Matsushima, T. Suzuki, Preparation of zinc ferrite in the presence of carbon material and its application to hot-gas cleaning, Fuel 83 (2004) 661–669.

[8] J.A. Toledo-Antonio, N. Nava, M. Martinez, X. Bokhimi, Correlation between the magnetism of non-stoichiometric zinc ferrites and their catalytic activity for oxidative dehydrogenation of 1-butene, Applied Catalysis A 234 (2002) 137–144.

[9] F. Papa, L. Patron, O. Carp, C. Paraschiv, B. Ioan, Catalytic activity of neodymium substituted zinc ferrites for oxidative conversion of methane, Journal of Molecular Catalysis A: Chemical 299 (2009) 93–97.

[10] M. Kobayashi, H. Shirai, M. Nunokawa, Estimation of multiple-cycle desulfurization performance for extremely low-concentration sulfur removal with sorbent containing zinc ferrite–silicon dioxide composite powder, Energy Fuels 16 (2002) 1378–1386.

[11] R. Lebourgeois, C. Coillot, Mn–Zn ferrites for magnetic sensor in space applications, Journal of Applied Physics 103 (2008) 07E510.

[12] E. Matijevic, Science of Ceramic Chemical Processing, Wiley, New York, 1986.

[13] R. Klimkiewicz, J. Wolska, A. Przepiera, K. Przepiera, M. Jabonski, S. Lenart, The zinc ferrite obtained by oxidative precipitation method as a catalyst in n-butanol conversion, Materials Research Bulletin 44 (2009) 15–20.

[14] J. Zhao, L. Mi, H. Hou, X. Shi, Y. Fan, The preparation of zinc ferrite nanorods by using single ferrocenyl complex as precursor, Materials Letters 61 (2007) 4196–4198.

[15] M. Sivakumar, A. Towata, K. Yasui, T. Tuziuti, Y. Iida, A new ultrasonic cavitation approach for the synthesis of zinc ferrite nanocrystals, Current Applied Physics 6 (2006) 591–593.

[16] I. Mohai, J. Szepvolgyi, I. Bertoti, M. Mohai, J. Gubicza, T. Ungar, Thermal plasma synthesis of zinc ferrite nanopowders, Solid State Ionics 141–142 (2001) 163–168.

[17] P. Yadoji, R. Peelamedu, D. Agrawal, R. Roy, Microwave sintering of Ni–Zn ferrites: comparison with conventional sintering, Materials Science and Engineering B 98 (2003) 269–278.

[18] N.C.S. Selvam, R. Thinesh Kumar, K. Yogeenth, L. John Kennedy, G. Sekaran, J. Judith Vijaya, Simple and rapid synthesis of cadmium oxide (CdO) nanospheres by a microwave-assisted combustion method, Powder Technology 211 (2011) 250–255.

[19] X.Y. Li, Y. Hou, Q.D. Zhao, L.Z. Wang, A general, one-step and template-free synthesis of sphere-like zinc ferrite nanostructures with enhanced photo catalytic activity for dye degradation, Journal of Colloid and Interface Science 358 (2011) 102–108.

[20] O.M. Lemine, M. Bououdina, M. Sajieddine, A.M. Al-Saie, M. Shafi, A. Khatab, M. Alhilali, M. Henini, Synthesis, structural, magnetic and optical properties of nanocrystalline $ZnFe_2O_4$, Physica B 406 (2011) 1989–1994.

[21] R. Thinesh Kumar, N.C.S. Selvam, C. Ragupathi, L. John Kennedy, J. Judith Vijaya, Synthesis, characterization and performance of porous Sr(II)-added $ZnAl_2O_4$ nanomaterials for optical and catalytic applications, Powder Technology 224 (2012) 147–154.

[22] M.A. Ashraf, A.H. Bhuiyan, M.A. Hakim, M.T. Hossain, Microstructure and electrical properties of Ho_2O_3 doped Bi_2O_3-based ZnO varistor ceramics, Physica B 405 (2010) 3770–3774.

[23] H. Ehrhardta, S.J. Campbell, M. Hofmann, Structural evolution of ball-milled $ZnFe_2O_4$, Journal of Alloys and Compounds 339 (2002) 255–260.

[24] M. Atif, M. Nadeem, R. Grossinger, R.S. Turtelli, Studies on the magnetic, magnetostrictive and electrical properties of sol–gel synthesized Zn doped nickel ferrite, Journal of Alloys and Compounds 509 (2011) 5720–5724.

[25] A. Kumar, Annveer, M. Arora, M.S. Yadav, R.P. Pant, Induced size effect on Ni doped nickel zinc ferrite nanoparticles, Physics Procedia 9 (2010) 20–23.

[26] A. Kumar, A. Singh, M.S. Yadav, M. Arora, R.P. Pant, Finite size effect on Ni doped nanocrystalline $Ni_xZn_{1-x}Fe_2O_4$ ($0.1 \leq x \leq 0.5$), Thin Solid Films 519 (2010) 1056–1058.

[27] A. Azam, Microwave assisted synthesis and characterization of Co doped Cu ferrite nanoparticles, Journal of Alloys and Compounds 540 (2012) 145–153.

[28] T. Tangcharoen, A. Ruangphanit, W. Pecharapa, Structural and magnetic properties of nanocrystalline zinc-doped metal ferrites (metal=Ni; Mn; Cu) prepared by sol–gel combustion method,

Ceramics International, http://dx.doi.org/10.1016/j.ceramint.2012.10.069.

[29] I. Sharifi, H. Shokrollahi, Nanostructural, magnetic and Mossbauer studies of nanosized $Co_{1-x}Zn_xFe_2O_4$ synthesized by co-precipitation, Journal of Magnetism and Magnetic Materials 324 (2012) 2397–2403.

[30] C. Upadhyay, Cation distribution in nanosized Ni–Zn ferrites, Journal of Applied Physics 95 (2004) 5746–5746.

[31] I.H. Gul, W. Ahmed, A. Maqsood, Electrical and magnetic characterization of nanocrystalline Ni–Zn ferrite synthesis by co-precipitation route, Journal of Magnetism and Magnetic Materials 320 (2008) 270–275.

[32] N. Kumar, G. Khurana, A. Gaur, R.K. Kotnala, Observation of superparamagnetism in ultrafine $Zn_xFe_{1-x}Fe_2O_4$ nanocrystals synthesized by co-precipitation method, Materials Chemistry and Physics 134 (2012) 783–788.

[33] H. Zhu, D. Yang, G. Yu, H. Zhang, K. Yao, Hydrothermal synthesis of Zn_2SnO_4 nanorods in the diameter regime of sub-5 nm and their properties, Nanotechnology 17 (2006) 2386.

[34] M. Parthibavarman, V. Hariharan, C. Sekar, High-sensitivity humidity sensor based on SnO_2 nanoparticles synthesized by microwave irradiation method, Materials Science and Engineering C 31 (2011) 840–844.

[35] N. Kislova, S.S. Srinivasan, Y. Emirov, E.K. Stefanakos, Optical absorption red and blue shifts in $ZnFe_2O_4$ nanoparticles, Materials Science and Engineering B 153 (2008) 70–77.

[36] R.B. Kale, C.D. Lokhande, Influence of air annealing on the structural, optical and electrical properties of chemically deposited CdSe nano-crystallites, Applied Surface Science 223 (2004) 343–351.

[37] A.V. Dijken, E.A. Meulenkamp, D. Vanmaekelbergh, A. Meijerink, Identification of the transition responsible for the visible emission in ZnO using quantum size effects, Journal of Luminescence 90 (2000) 123–128.

[38] A.V. Dijken, E.A. Meulenkamp, D. Vanmaekelbergh, A. Meijerink, The luminescence of nanocrystalline ZnO particles: the mechanism of the ultraviolet and visible emission, Journal of Luminescence 87 (2000) 454–456.

[39] A.K. Srivastava, M. Deepa, N. Bahadur, M.S. Goyat, Influence of Fe doping on nanostructures and photoluminescence of sol–gel derived ZnO, Materials Chemistry and Physics 114 (2009) 194–198.

[40] D. Gao, Z. Shi, Y. Xu, J. Zhang, G. Yang, J. Zhang, X. Wang, D. Xue, Synthesis, magnetic anisotropy and optical properties of preferred oriented zinc ferrite nanowire arrays, Nanoscale Research Letters 5 (2010) 1289–1294.

[41] J. Li, Z. Huang, D. Wu, G. Yin, X. Liao, J. Gu, D. Han, Preparation and protein detection of Zn-Ferrite film with magnetic and photoluminescence properties, Journal of Physical Chemistry C 114 (2010) 1586–1592.

[42] P.H. Borse, J.S. Jang, S.J. Hongand, J.S. Lee, J.H. Jung, T.E. Hong, C.W. Ahn, E.D. Jeong, K.S. Hong, J.H. Yoon, H.G. Kim, Photocatalytic hydrogen generation from water–methanol mixtures using nanocrystalline $ZnFe_2O_4$ under visible light irradiation, Journal of the Korean Physical Society 55 (2009) 1472–1477.

[43] A. Van Dijken, E.A. Meulenkamp, D. Vanmaekelbergh, A. Meijerink, Identification of the transition responsible for the visible emission in ZnO using quantum size effects, Journal of Luminescence 90 (2000) 123–128.

[44] S. Ayyappan, S. Philip Raja, C. Venkateswaran, J. Philip, B. Raj, Room temperature ferromagnetism in vacuum annealed $ZnFe_2O_4$ nanoparticles, Applied Physics Letters 96 (2010) 143106.

[45] G.F. Goya, H.R. Rechenberg, Ionic disorder and Neel temperature in $ZnFe_2O_4$ nanoparticles, Journal of Magnetism and Magnetic Materials 196–197 (1999) 191–192.

[46] T. Yamanaka, M. Okita, Magnetic properties of the Fe_2SiO_4–Fe_3O_4 spinel solid solutions, Physics and Chemistry of Minerals 28 (2001) 102–109.

[47] M. Bohra, S. Prasad, N. Kumar, D.S. Misra, S.C. Sahoo, N. Venkataramani, R. Krishnan, Large room temperature magnetization in nanocrystalline zinc ferrite thin films, Applied Physics Letters 88 (2006) 262506.

[48] S. Nakashima, K. Fujita, K. Tanaka, K. Hirao, T. Yamamoto, I. Tanaka, Thermal annealing effect on magnetism and cation distribution in disordered $ZnFe_2O_4$ thin films deposited on glass substrates, Journal of Magnetism and Magnetic Materials 310 (2007) 2543.

[49] Y. Changwa, Z. Qiaoshi, G.F. Goya, T. Torres, L. Jinfang, W. Haiping, G. Mingyuan, Z. Yuewu, W. Youwen, J.Z. Jiang, $ZnFe_2O_4$ nanocrystals: synthesis and magnetic properties, Journal of Physical Chemistry C 111 (2007) 12274–12278.

[50] P.P. Hankare, R.P. Patil, A.V. Jadhav, K.M. Garadkar, R. Sasikala, Enhanced photocatalytic degradation of methyl red and thymol blue using titania–alumina–zinc ferrite nanocomposite, Applied Catalysis B: Environmental 107 (2011) 333–339.

[51] A.E. Berkowitz, R.H. Kodama, S.A. Makhlouf, F.T. Parker, F.E. Spada, E.J. McNiff Jr, S. Foner, Anomalous properties of magnetic nanoparticles, Journal of Magnetism and Magnetic Materials 196–197 (1999) 591–594.

[52] V. Sepelak, L. Wilde, U. Steinike, K.D. Becker, Thermal stability of the non-equilibrium cation distribution in nanocrystalline high-energy milled spinel ferrite, Materials Science and Engineering A 865 (2004) 375–377.